Adapting the Lagrangian speckle model estimator for endovascular elastography: Theory and validation with simulated radio-frequency data

Roch L. Maurice
Laboratory of Biorheology and Medical Ultrasonics, Research Center, University of Montreal Hospital, Montreal, Canada

Jacques Ohayon
Laboratory TIMC-IMAG, UMR CNRS 5525, Institut A. Bonniot, 38706 La Tronche, France

Gérard Finet
Department of Hemodynamics, Cardiovascular Hospital, Claude Bernard University, Lyon, France

Guy Cloutier[a)]
Laboratory of Biorheology and Medical Ultrasonics, Research Center, University of Montreal Hospital, Montreal, Canada

(Received 3 October 2003; revised 17 May 2004; accepted 17 May 2004)

Intravascular ultrasound (IVUS) is known to be the reference tool for preoperative vessel lesion assessments and for endovascular therapy planning. Nevertheless, IVUS echograms only provide subjective information about vessel wall lesions. Since changes in the vascular tissue stiffness are characteristic of vessel pathologies, catheter-based endovascular ultrasound elastography (EVE) has been proposed in the literature as a method for outlining the elastic properties of vessel walls. In this paper, the Lagrangian Speckle Model Estimator (LSME) is formulated for investigations in EVE, i.e., using a polar coordinate system. The method was implemented through an adapted version of the Levenberg-Marquardt minimization algorithm, using the optical flow equations to compute the Jacobbian matrix. The theoretical framework was validated with simulated ultrasound rf data of mechanically complex vessel wall pathologies. The results, corroborated with Ansys finite element software, demonstrated the potential of EVE to provide useful information about the heterogeneous nature of atherosclerotic plaques. © *2004 Acoustical Society of America.*
[DOI: 10.1121/1.1771615]

PACS numbers: 43.80.Vj [FD] Pages: 1276–1286

I. INTRODUCTION

Intravascular elastography, or equivalently endovascular elastography (EVE), was introduced in the late nineties as a new imaging modality that aims to outline the elastic properties of vessel walls. In EVE, the vascular tissue is compressed by applying a force from within the lumen. Indeed, the compression can be induced by the normal cardiac pulsation or by using a compliant intravascular angioplasty balloon. The feasibility of EVE was investigated *in vitro* with phantom studies (de Korte *et al.*, 1997) and with excised vessels (de Korte *et al.*, 1998 and 2000a; Brusseau *et al.*, 2001; Wan *et al.*, 2001), and *in vivo* on human coronary arteries (de Korte *et al.*, 2000b). Interestingly, it was demonstrated that EVE could provide information that is occlusive to intravascular ultrasound (IVUS) images.

However, *in vivo*, the position of the catheter in the lumen is generally off center and may move in response to the flow pulsatility. Moreover, the lumen geometry is often not perfectly circular. In such conditions, the ultrasound beam does not run parallel with tissue displacements, and appropriate coordinate systems are required to model both the ultrasound propagation and the tissue motion. Owing to that, (one-dimensional) 1-D-motion estimators may not be optimal for EVE applications. Ryan and Foster (1997) then proposed to use a 2-D correlation-based speckle tracking method to compute vascular elastograms. Additionally to a 2-D correlation-based estimator, Shapo *et al.* (1996a, 1996b) proposed the use of an angioplasty balloon to stabilize the catheter in the vessel lumen. Those phantom investigations tended to demonstrate the feasibility of EVE in the presence of motion artifacts, and its potential to provide new diagnosis information that may help in the functional assessment of atherosclerosis.

Another strategy was proposed by de Korte *et al.* (2000b) to minimize artifacts due to catheter motion. It consisted in using pre- and post-motion images near end-diastole for a pressure differential of approximately 5 mm Hg. The computed *in vivo* elastograms could detect an area composed of hardened material, which was corroborated with IVUS B-scans that revealed a large calcified area. This last method may become a standard procedure if one considers EVE without the use of an angioplasty balloon.

So far, EVE appears a very attractive and promising tool to characterize the mechanical properties of vessel walls. However, in return, it is potentially limited by motion arti-

[a)]Director of the Laboratory of Biorheology and Mecidal Ultrasonics, Electronic mail: guy.cloutier@umontreal.ca

 0001-4966/2004/116(2)/1276/11/$20.00 © 2004 Acoustical Society of America

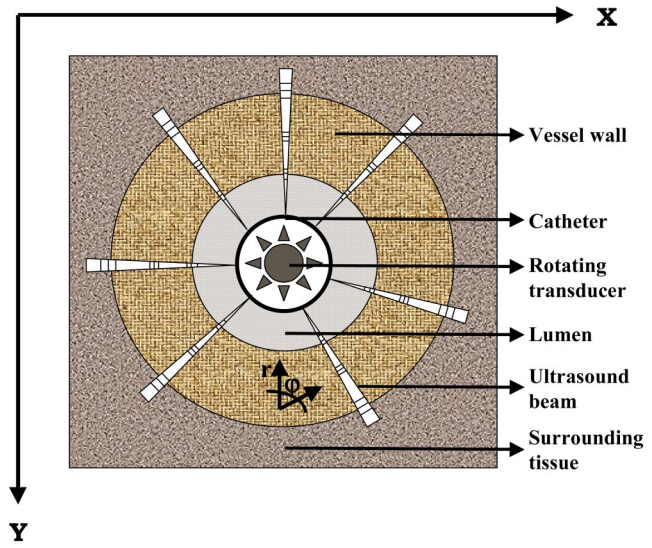

FIG. 1. A schematic illustration of the image acquisition process in IVUS and EVE. The transducer is placed at the tip of the catheter and cross-sectional imaging of the vessel is generated by sequentially sweeping the ultrasound beam over an angle of 360°. In this ideal situation, the ultrasound beam runs parallel with the vascular tissue motion, i.e., in the (r,φ) coordinate system.

facts. Furthermore, it is also limited by the heterogeneous nature of the vascular tissue and of the plaque itself that may induce very complex tissue deformations (nonrigid rotation, scaling, shear, etc.). Most of the current *elastographic* methods use correlation techniques to assess tissue motion and may not be optimal to investigate such complex strain patterns. In this paper we propose an adaptation of the Lagrangian Speckle Model Estimator (LSME) for strain computation in EVE, i.e., for a formulation in a polar coordinate system. The method was implemented through an adapted version of the Levenberg-Marquardt minimization algorithm, using the optical flow equations to compute the Jacobbian matrix. While the full 2-D polar strain tensor was assessed, only the radial strain parameter is displayed in this paper. The theoretical framework was validated with simulated ultrasound rf data of mechanically complex vessel wall pathologies. Namely, one *idealized* and one *realistic* plaque were investigated. Whereas the former allowed validating the potential of the method to differentiate between hard and soft vascular tissues, the latter showed its potential to characterize the heterogeneous nature of atherosclerosis. Interestingly, it is worth noting that a polar image-formation model that simulates the spatial variation of the ultrasound beam with depth was also introduced.

This paper is organized as follows. In Sec. II A, the forward problem in EVE is addressed; it is followed by the derivation of the tissue motion estimator in Sec. II B, and by the biomechanical simulations of the vessel walls in Sec. II C. Results are presented in Sec. III, while in Secs. IV and V we discuss the results and draw conclusions and perspectives to this work.

II. METHODOLOGY

Endovascular elastography (EVE) is a catheter-based modality, which gives insights about mechanical properties of the vessel wall. Following the example of IVUS, and as schematically illustrated in Fig. 1, the transducer is placed at the tip of the catheter and cross-sectional imaging of a vessel is generated by sequentially sweeping the ultrasound beam over a 360° angle. Mechanical parameters (radial strain, in this case) are estimated from analyzing the kinematics of the vascular tissue during the cardiac cycle (or in response to an angioplasty-balloon push).

A. The forward problem in EVE

1. The polar static-image-formation model

The image-formation model is for a rotating beam (single element or an array transducer system) and is thus expressed in polar coordinates. It is based on previous works by Bamber and Dickinson (1980). Such a model was used by Meunier and Bertrand (1995) to study speckle dynamics; it was also considered to investigate speckle motion artifacts (Kallel and Bertrand, 1994; Maurice and Bertrand, 1999b). Under assumptions such as space-invariance of the imaging system, and plane strain conditions for the motion (that is no transverse motion is involved), the following simple 2-D model was used (Maurice and Bertrand, 1999b):

$$I'(x,y)=h'(x,y)\otimes z'(x,y), \tag{1}$$

where $I'(x,y)$ is the radio-frequency (rf) image, $h'(x,y)$ is the point-spread function (PSF) of the ultrasound system, $\otimes$ is the 2-D convolution operator, and $z'(x,y)$ is a function representing the acoustic impedance variations, which was modeled as a white Gaussian noise (random distribution of uncorrelated scatterers within the region of interest). As it will be seen further in this section, the notation "′" is only for convenience and it does not refer to any mathematical operator.

Because the speckle dimension varies with depth for polar scan systems such as the one described in Fig. 1, Eq. (1) is valid only for small regions of interest (ROI). Accordingly, the linear image-formation model is formulated using the superposition integral, given by

$$I(r,\varphi)=\int\int h(r,\varphi,r',\varphi')z(r',\varphi')r'\,dr'\,d\varphi', \tag{2}$$

where r and φ are the radial (depth) and angular coordinates, respectively; $I(r,\varphi)$, $h(r,\varphi)$, and $z(r,\varphi)$ are the polar rf image, polar PSF, and the acoustic impedance function mapped in polar coordinates, respectively; (r',φ') is the position of the "point object" used to define the polar PSF. Furthermore, for a polar scan system, $h(r,\varphi)$ can be considered angular-position invariant; therefore, Eq. (2) becomes

$$I(r,\varphi)=\int\int h(r,r',\varphi-\varphi')z(r',\varphi')r'\,dr'\,d\varphi'. \tag{3}$$

It is convenient to model the PSF as a 1-D cosine modulated by a 2-D Gaussian envelope; that is a simple approximation of the far field PSF. The mathematical formulation can be expressed as

$$h(r,r',\varphi-\varphi') = e^{-((r-r')^2/2\sigma_r^2+(\varphi-\varphi')^2/2\sigma_\varphi^2)} \times \cos\left(2\pi\frac{f_{\text{tr}}}{c/2}(r-r')\right), \quad (4)$$

where σ_r is a pulse length parameter; $\sigma_\varphi \equiv \sigma_\varphi(r)$ is a beam-width parameter;[b] f_{tr} and c are the transducer frequency and the sound velocity in soft tissue, respectively. For simplicity, it is assumed that $\sigma_\varphi(r)$ is a linear function of r; it is expressed as

$$\sigma_\varphi(r) = \frac{r}{R_L}\sigma_0, \quad r \geqslant R_L, \quad (5)$$

with R_L being the lumen radius and σ_0 the beam width at $r = R_L$. In such a situation, the beam forms a sector that linearly increases with depth through the vessel wall. It is important to notice that Eqs. (4) and (5) define a very simple approximation of the PSF in the far-field. In practice, the near field beam profile is more complex. However, it can be assumed that the transducer is positioned near the middle of the lumen, so that the vessel wall is not in the near field.[c] Additionally to the divergence of the ultrasound beam profile, the nonplanar nature of the wavefronts also raises the complexity of the polar scan model; this aspect was not modeled in the current study.

In theory, $\sigma_\varphi(r)$ is a continuous function of r. However, for simplification it will be considered as a piecewise constant function, the n partitioning regions being defined by the boundaries $0 = r_0 < r_1 < r_2 < \cdots \leqslant r_n$. For convenience, each partition will be denoted as P_i, that is,

$$P_i =]r_{i-1}, r_i], \quad i = 1,...,n. \quad (6)$$

Equation (6) defines an interval; the reversed left bracket means that r_0 (the first element of the interval) is excluded. A discrete approximation of $\sigma_\varphi(r)$ is then defined as follows:

$$\sigma_\varphi(r)\big|_{r\in P_i} \cong \sigma_\varphi(P_i) = \frac{\overline{P_i}}{R_L}\sigma_0, \quad (7)$$

where $\overline{P_i}$ is the mean radial distance of the interval P_i. Now, assuming that the PSF is locally depth-invariant, i.e., on each P_i, the linear model of Eq. (3) can be approximated by the following convolution form:

$$I(r,\varphi) \cong \sum_{i=1}^{n} I(P_i,\varphi) = \sum_{i=1}^{n} [h(P_i,\varphi) \otimes z(P_i,\varphi)], \quad (8)$$

with

$$h(P_i,\varphi) = h(r,\varphi)\big|_{r\in P_i} = e^{-(r^2/2\sigma_r^2+\varphi^2/2\sigma_\varphi(r)^2)} \cos\left(2\pi\frac{f_{\text{tr}}}{c/2}r\right).$$

While the continuity of $I(r,\varphi)$ at the boundaries of the partitions can be questioned, Eq. (8) presents a simple approximation model of a polar scan system. Figure 2 illustrates the implementation of such a model for a 20 MHz transducer with a 60% bandwidth at -3 dB and a beam width (width at half maximum $= 2.35 \times \sigma_0$) of 0.1 mm. $z(r,\varphi)$ is assumed to be a continuum. For the purpose of the simulations presented below, $z(r,\varphi)$ was simply obtained by generating a 2-D normally distributed random field. The lumen and the tissue surrounding the vessel were assumed to be, respectively, 2.5 and 1.67 times less echoic than the wall.

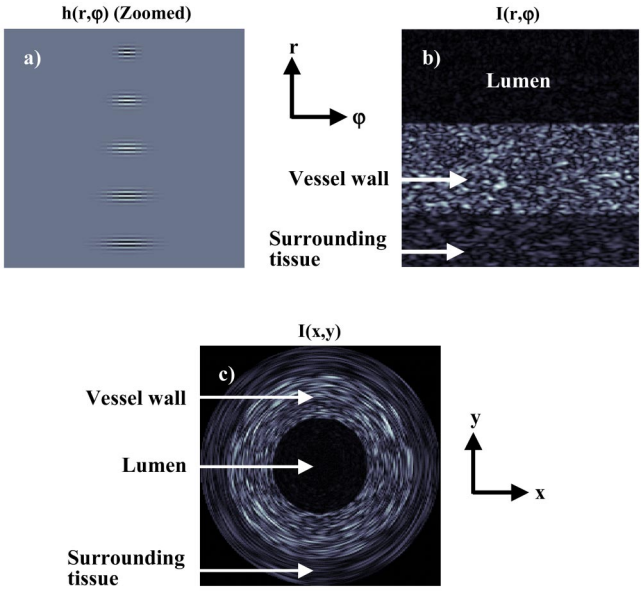

FIG. 2. Image-formation model for a 20 MHz polar scan system; (a) shows the beam profile as a function of depth; (b) presents the simulated polar B-mode image for an homogenous vessel section; (c) is the IVUS simulated image.

Figure 2(a) shows the beam profile as a function of depth. The beam width increases linearly, being minimal in the lumen and maximal in the surrounding tissue; the partition number n was set at 5. Figure 2(b) presents a simulated polar *B*-mode image for an homogenous vessel section, whereas Fig. 2(c) gives the equivalent IVUS image (in Cartesian coordinates).

2. The tissue-motion model

For a small ROI, tissue motion can be approximated by an affine transformation; this can be expressed in Cartesian coordinates as

$$\begin{bmatrix} p(x,y,t) \\ q(x,y,t) \end{bmatrix} = \underbrace{\begin{bmatrix} \theta_1 \\ \theta_4 \end{bmatrix}}_{\text{Tr}} + \underbrace{\begin{bmatrix} \theta_2 & \theta_3 \\ \theta_5 & \theta_6 \end{bmatrix}}_{\text{LT}} \begin{bmatrix} x \\ y \end{bmatrix}, \quad (9)$$

where θ_j is a function of time t ($\theta_j(t)$). Equation 9 expresses a translation of the center of the ROI (vector $[T_r]$) and a linear geometrical transformation of coordinates (matrix $[LT]$).[d] It can also be seen as trajectories that describe a tissue motion in a region of constant strain (Maurice and Bertrand, 1999a). Strain is usually defined in terms of the gradient of a displacement field; since $p(x,y,t)$ and $q(x,y,t)$ represent the new position of a point (x,y), the (u_x,u_y) components of the displacement vector in the (x,y) coordinate system are given by

$$\begin{bmatrix} u_x \\ u_y \end{bmatrix} = \begin{bmatrix} p(x,y,t)-x \\ q(x,y,t)-y \end{bmatrix} = \begin{bmatrix} \theta_1 \\ \theta_4 \end{bmatrix} + \Delta \begin{bmatrix} x \\ y \end{bmatrix}, \quad (10)$$

with

$$\Delta=\begin{bmatrix}\theta_2-1 & \theta_3\\ \theta_5 & \theta_6-1\end{bmatrix}.$$

In the above equation, Δ can be defined as the Cartesian deformation matrix. The ϵ_{ij}, which are the components of the strain tensor ϵ, are expressed in terms of the Δ_{ij} components as

$$\epsilon_{ij}(t)=\tfrac{1}{2}[\Delta_{ij}(t)+\Delta_{ji}(t)]. \tag{11}$$

Furthermore, the radial and tangential components of the displacement vector (u_r,u_φ) in the (r,φ) coordinate system are, respectively, given as

$$u_r=\sqrt{u_x^2+u_y^2},$$

$$u_\varphi=\arctan\left(\frac{u_y}{u_x}\right),$$

with

$$u_x\equiv u_x(x(r,\varphi),y(r,\varphi)) \quad \text{and} \quad u_y\equiv u_y(x(r,\varphi),y(r,\varphi)). \tag{12}$$

The polar deformation matrix, labeled as $\xi(t)$, then can be derived from Eqs. (12) and (10); it is given as

$$\xi(t)=\begin{bmatrix}\frac{\partial u_\varphi}{\partial\varphi} & \frac{\partial u_\varphi}{\partial r}\\ \frac{\partial u_r}{\partial\varphi} & \frac{\partial u_r}{\partial r}\end{bmatrix}$$

$$=\begin{bmatrix}\frac{\partial u_\varphi}{\partial u_x} & \frac{\partial u_\varphi}{\partial u_y}\\ \frac{\partial u_r}{\partial u_x} & \frac{\partial u_r}{\partial u_y}\end{bmatrix}\begin{bmatrix}\frac{\partial u_x}{\partial x} & \frac{\partial u_x}{\partial y}\\ \frac{\partial u_y}{\partial x} & \frac{\partial u_y}{\partial y}\end{bmatrix}\begin{bmatrix}\frac{dx}{d\varphi} & \frac{dx}{dr}\\ \frac{dy}{d\varphi} & \frac{dy}{dr}\end{bmatrix}$$

$$=\begin{bmatrix}\frac{\partial u_\varphi}{\partial u_x} & \frac{\partial u_\varphi}{\partial u_y}\\ \frac{\partial u_r}{\partial u_x} & \frac{\partial u_r}{\partial u_y}\end{bmatrix}\Delta\begin{bmatrix}\frac{dx}{d\varphi} & \frac{dx}{dr}\\ \frac{dy}{d\varphi} & \frac{dy}{dr}\end{bmatrix}, \quad \text{with} \begin{cases}x=r\cos\varphi,\\ y=r\sin\varphi\end{cases}. \tag{13}$$

The LSME computes the full 2-D-strain tensor $\xi(t)$. However, for the purpose of this paper, only the map of the $\xi_{rr}(=\epsilon_{rr})$ component (the radial strain, labeled in EVE as the elastogram) is displayed. For small deformations, the elastogram is expected to provide cartography of relative tissue stiffness inside the vessel wall. This assumption holds, for example, when pre- and post-motion rf images are acquired for a small pressure gradient, i.e., at the end-diastole. ξ_{rr} can be expressed as a function of the Cartesian deformation matrix (Δ) as

$$\xi_{rr}(t)=\frac{\partial u_r}{\partial r}=\begin{bmatrix}\frac{\partial u_r}{\partial u_x} & \frac{\partial u_r}{\partial u_y}\end{bmatrix}\Delta\begin{bmatrix}\cos\varphi\\ \sin\varphi\end{bmatrix}. \tag{14}$$

3. The polar dynamic-image-formation model

The 2-D polar dynamic-image-formation model for an in-plane tissue motion is now derived. It is worth remembering that $z(r,\varphi)$ is a map of the acoustic impedance variations $z'(x,y)$ in polar coordinates, which can mathematically be expressed as

$$z(r,\varphi)=z'(x,y)\big|_{\substack{x=r\cos\varphi\\ y=r\sin\varphi}}. \tag{15}$$

The affine transformation on $z'(x,y)$ can be set by only changing the (x,y) coordinates. Without loss of generality, it is assumed that translation is absent, and $[T_r]$ in Eq. (9) can thus be neglected. It is also interesting to notice that impressing $[LT]$ on the tissue to simulate deformation requires the computation of the inverse transformation $[LT^{-1}]$ on the coordinates. Hence, for an (r,φ) in-plane motion, the 2-D rf polar dynamic-image-formation model at time t becomes

$$I(r,\varphi,t)\cong\sum_{i=1}^{n} I(P_i,\varphi,t)$$

$$=\sum_{i=1}^{n}[h(P_i,\varphi)\otimes z_{LT_p^{-1}}(P_i,\varphi)],$$

with

$$z_{LT_p^{-1}}(P_i,\varphi)=z_{LT_p^{-1}}(r,\varphi)\big|_{r\in P_i}=z'_{LT^{-1}}(x,y)\big|_{\substack{x=r\cos\varphi\\ y=r\sin\varphi}}. \tag{16}$$

In Eq. (16), $z'_{LT^{-1}}(x,y)$ indicates a change in coordinates for the function $z'(x,y)$; that change involves the 2×2 matrix $[LT^{-1}]$. Similarly, $z_{LT_p^{-1}}(P_i,\varphi)$ indicates a change in coordinates for the function $z(P_i,\varphi)$ where the 2×2 matrix $[LT_p^{-1}]$ is involved. Implicitly, this means that $[LT]$ (as well as $[LT_p]$) is invertible. This assumption is valid for an incompressible continuum.

B. Tissue motion estimation in EVE

1. Lagrangian speckle image (LSI)

Vascular tissue may rotate, shear, stretch, or compress in the measurement plane. Such kinematics set a fundamental limitation to correlation-based tissue motion estimators, if they are not appropriately compensated for. In conventional elastography, where an external compression is induced, Ophir *et al.* (1999) proposed to partially compensate for such decorrelation by using temporal stretching of the post-motion signals, whereas Chaturvedi *et al.* (1998a,b) proposed the 2-D-companding method. Interestingly, the Lagrangian speckle image (LSI) was introduced to describe ultrasound signals compensated for tissue motion (Maurice and Bertrand, 1999a). For instance, in the dynamic image-formation model of Eq. (16), tissue motion is modeled by applying the linear transformation matrix $[LT_p^{-1}]$ to $z(r,\varphi)$. Hence, the motion-compensated image, said the LSI, is obtained through applying $[LT_p]$ (the inverse of $[LT_p^{-1}]$) to a post-motion rf image at time t given by $I(r,\varphi,t)$. For the polar dynamic image-formation model given by Eq. (16), the LSI (noted as I_{Lag}) is then expressed as

$$I_{\text{Lag}}(r,\varphi,t)=[I(r,\varphi,t)]_{LT_p}$$

$$\cong\left[\sum_{i=1}^{n} h(P_i,\varphi)\otimes z_{LT_p^{-1}}(P_i,\varphi)\right]_{LT_p}$$

$$=\sum_{i=1}^{n}[h_{LT_p}(P_i,\varphi)\otimes z(P_i,\varphi)|LT_p|]. \tag{17}$$

In the above equation, $|LT_p|$ is the determinant of the matrix $[LT_p]$.

2. The Lagrangian speckle model and the minimization problem

As described in Maurice and Bertrand (1999a), the motion-compensated rf image (LSI) directly involves the Lagrangian description of motion. For instance, it is expressed in Eq. (17) that the LSI brings back material points to the positions where they originally stood. Accordingly, a convenient model to formulate the LSI can be given as

$$I(r,\varphi,0) = I_{\mathrm{Lag}}(r,\varphi,t) + \Re(r,\varphi,t) = [I(r,\varphi,t)]_{LT_p} + \Re(r,\varphi,t), \quad (18)$$

where $\Re(r,\varphi,t)$ can be seen as an error term. The mathematical model for a tissue motion estimator then can be formulated as

$$\begin{aligned} &\underset{LT_p}{\mathrm{MIN}} \|I(r,\varphi,0) - [I(r,\varphi,t)]_{LT_p}\|^2 \\ &= \underset{LT_p}{\mathrm{MIN}} \|I(r,\varphi,0) - I_{\mathrm{Lag}}(r,\varphi,t)\|^2 \\ &= \underset{LT_p}{\mathrm{MIN}} \|\Re(r,\varphi,t)\|^2. \end{aligned} \quad (19)$$

The minimum is obtained using the appropriate $[LT_p]$. It is worth remembering that $[LT_p]$ is a linear transformation matrix; it maps the Cartesian trajectories [Eq. (9)] in a polar coordinate system. However, for a small ROI $(\Delta r, \Delta\varphi)$ that is far from the vessel lumen center, motion equivalently can be investigated using either a polar or a Cartesian coordinate system. In other words, the following approximation can be done to compute the elastogram:

$$\xi \cong LT - I, \quad (20)$$

where I is the 2-D-identity matrix.

3. The Levenberg-Marquardt nonlinear minimization

Several gradient-based methods exist to numerically solve minimization problems as given by Eq. (19). Here, tissue motion was assessed by using the Levenberg-Marquardt method (L&M) (Levenberg, 1963; Marquardt, 1944). As presented in Appendix A, at the kth iteration, the L&M regularized inversion was implemented as

$$\vec{\Delta\theta}^k = [J_{k-1}^T J_{k-1} + \lambda_k I]^{-1} J_{k-1}^T (\vec{I}_0 - \vec{I}_{\mathrm{Lag}}(\vec{\theta}^{k-1})), \quad (21)$$

where $\vec{\Delta\theta}^k$ is a vector of increments used to update the Lagrangian images ($\vec{\Delta\theta}^k$ is also known in the literature as the step size); $[J_{k-1}]$ is the Jacobian matrix; T designates the transpose operator; λ_k is a non-negative scalar, I is the identity matrix; $I_0(r,\varphi,0)$ and $I_{\mathrm{Lag}}(r,\varphi,t)$ are rewritten as I_0 and $I_{\mathrm{Lag}}(\vec{\theta})$, respectively; and $\vec{\theta}$ is the vectorization of $[LT_p]$.

4. The optical flow equations and the Jacobian matrix

The optical flow equations, or material derivatives, give a relationship between measures in Eulerian and Lagrangian coordinate systems, respectively (Horn, 1986). For instance, $I_{\mathrm{Lag}}(\vec{\theta}^{k-1})$ can be seen as a function that describes a material property. Under such an assumption, as presented in Appendix B, the full expression for the 6 components of the Jacobian matrix $[J_{k-1}]$ [Eq. (21)] is given as

$$\frac{\partial I_{\mathrm{Lag}}(\vec{\theta}^{k-1})}{\partial\vec{\theta}} \cong \frac{\partial I(\vec{\theta}^{k-1})}{\partial\vec{\theta}} = -\left\{\frac{\partial I}{\partial x}, \frac{\partial I}{\partial x}x, \frac{\partial I}{\partial x}y, \frac{\partial I}{\partial y}, \frac{\partial I}{\partial y}x, \frac{\partial I}{\partial y}y\right\}. \quad (22)$$

Equation (22) was implemented to compute the Jacobian matrix required to solve the minimization problem of Eq. (19).

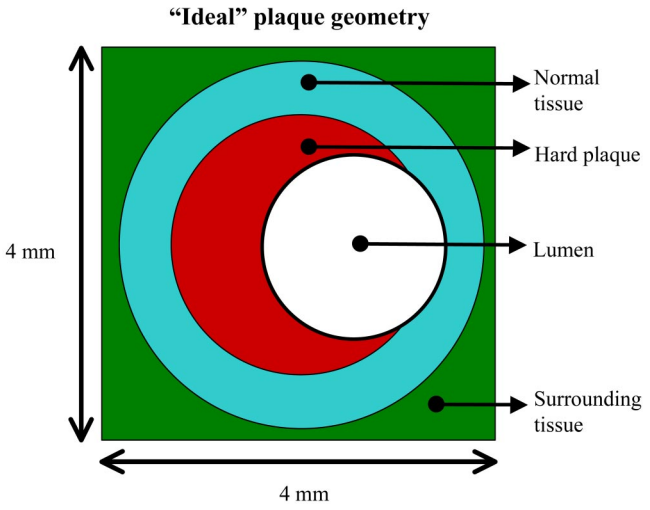

FIG. 3. Schematic representation of an "ideal" plaque. The Young's modulus for the normal vascular tissue was 80 kPa, while the plaque (three times stiffer) was set at 240 kPa. To emulate boundary conditions as provided by the surrounding environment, the Young's modulus for the surrounding tissue was set at 1000 kPa.

C. Biomechanical simulations of vessel wall kinematics

1. Model design and image analysis

The computational structural analysis was performed on one simulated idealized coronary plaque (Fig. 3), and on a model created from measurements made of a typical composite plaque identified from an *in vivo* IVUS image [Fig.

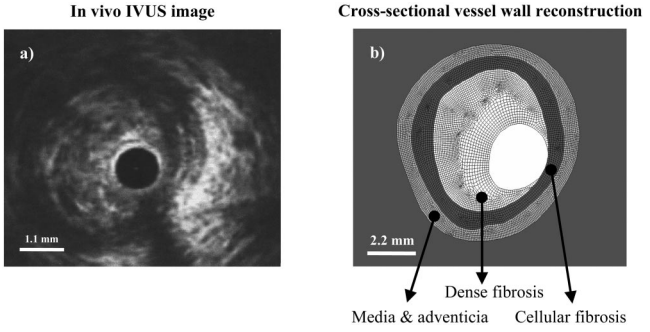

FIG. 4. (a) *In vivo* IVUS cross-sectional image of a coronary plaque; (b) 2-D finite element mesh of the unloaded real geometry with spatial distribution of the plaque constituents. The Young's modulus for the healthy vascular tissue (or adventicia and media) was 80 kPa, while the dense fibrosis (three times stiffer) was set at 240 kPa, and the cellular fibrosis at 24 kPa (ten times softer than the dense fibrosis).

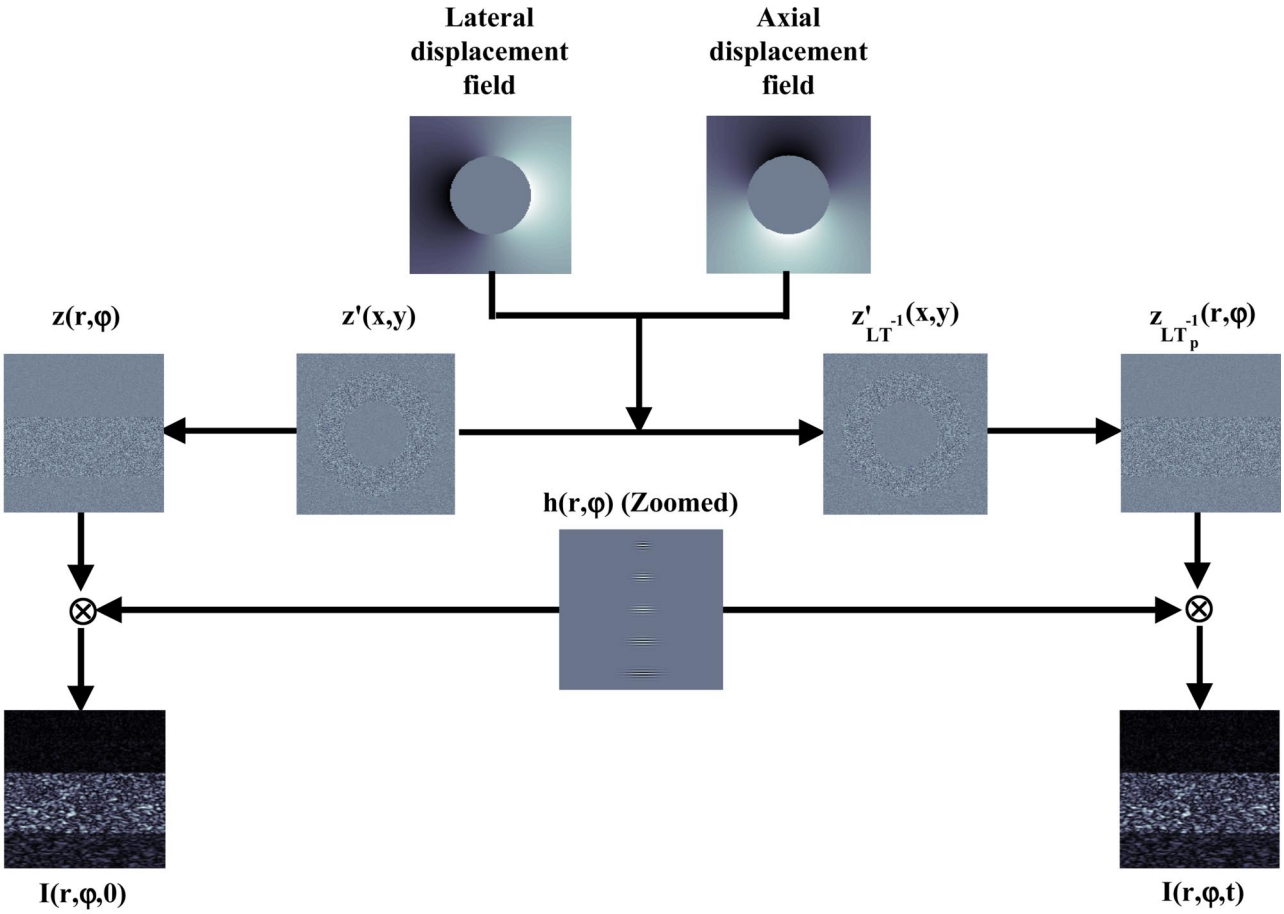

FIG. 5. Schematic implementation of the polar dynamic image-formation model.

4(a)]. Whereas the former allowed validating the potential of the method to differentiate between hard and soft vascular tissues, the latter investigated its potential to characterize the heterogeneous nature of atherosclerotic plaques, which is linked to the risk of rupture and thrombosis. The major difficulty in computational structural analysis based on *in vivo* imaging is to determine the unloaded physiological configuration of the artery, i.e., the configuration when the artery is subjected to no external load. This configuration has to be known for finite element (FE) simulations. To obtain this unloaded state, adenosine triphosphate (ATP) (Striadyne®, Wyeth France Laboratories) was injected to the patient,[e] as previously described by Ohayon *et al.* (2001). All contours in the IVUS image were manually traced [Fig. 4(b)]. These contours are those of the lumen border, media, adventicia, and plaque components (dense fibrosis and cellular fibrosis). The adventicia contour was added in the simulation and it had a mean thickness of 350 μm (Rioufol *et al.*, 1999), so as to take account of its protective role against any radial overstretching of the artery (Rachev, 1997). The various contours were digitized using the Un-Scan-It® software (Silk Scientific, Inc., Orem, UT).

2. Material properties

For the two models, the materials were considered as quasi-incompressible (Poisson ratios $\nu=0.49$) and isotropic with linear elastic properties. The Young's modulus for the healthy vascular tissue (or adventitia and media) was 80 kPa (Williamson *et al.*, 2003), while the dense fibrosis (much stiffer) was set at 240 kPa, and the cellular fibrosis (softer than the dense fibrosis) was chosen at 24 kPa (Ohayon *et al.*, 2001; Treyve *et al.*, 2003). Whereas the surrounding tissue was not investigated, the bulk boundary conditions, as it may eventually be provided by surrounding organs, were simulated by imbedding the vessel in a stiffer environment of 1000 kPa Young's modulus.[f]

3. Structural analysis

Finite element (FE) computations were performed using the ANSYS 5.7® software (Ansys, Inc., Cannonsburg, PA). Static simulations of coronary plaque under loading blood pressure were performed on the geometrical models previously described [Figs. 3 and 4(b)]. Nodal displacements were set to zero on the external boundaries of the surrounding tissue.

The various regions of the plaque components were then automatically meshed with triangular (6 nodes) and quadrangular (8 nodes) elements. The FE models were solved under the assumption of plane and of finite strains. The assumption of plane strain was made because axial stenosis dimensions were of at least the same order of magnitude as the radial dimensions of the vessel. Moreover, the assumption of finite deformation was required as the strain maps showed values up to 30% for physiological pressures (Loree *et al.*, 1992;

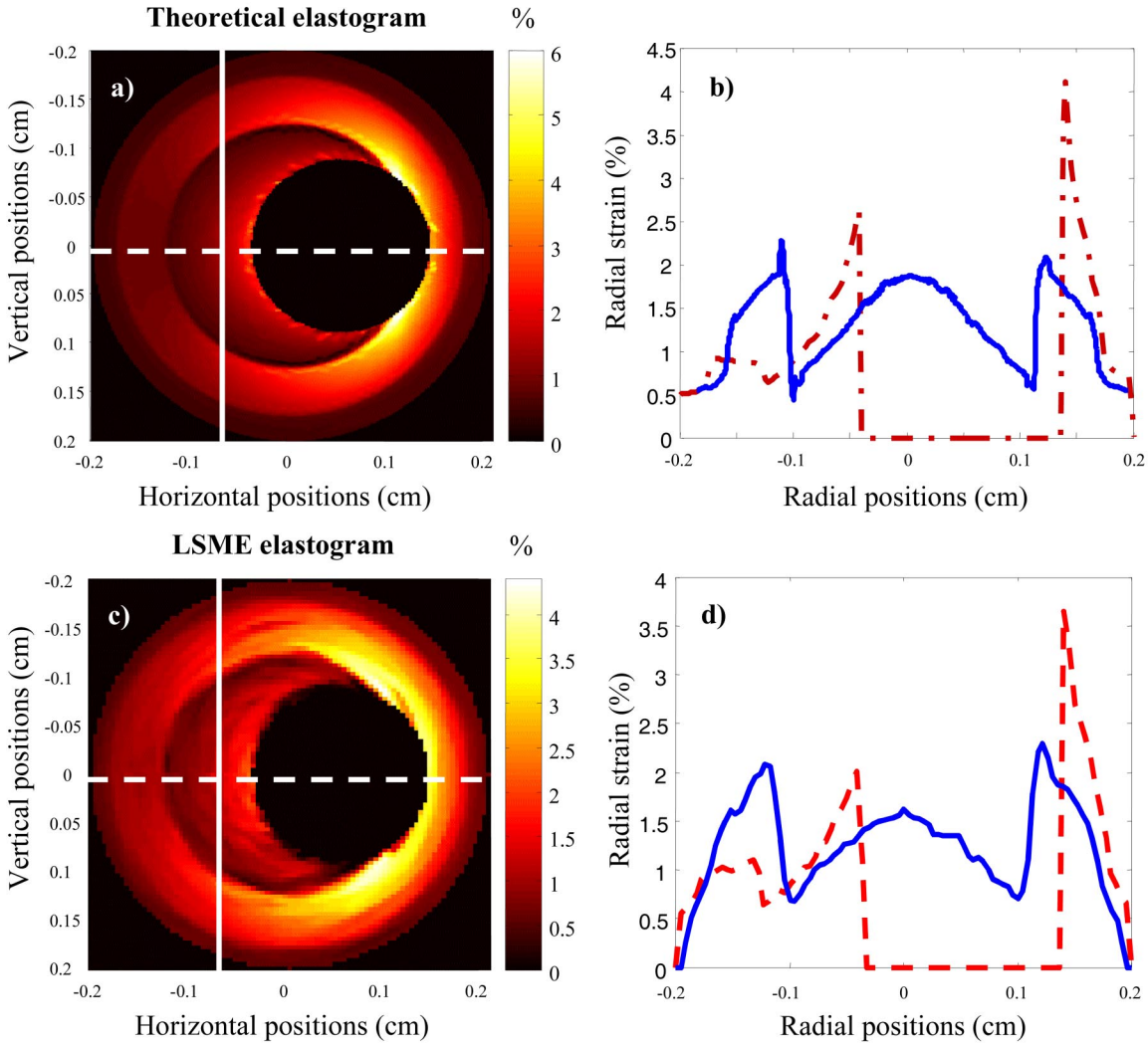

FIG. 6. (a) Theoretical radial strain elastogram, computed with Ansys FE software, for the idealized plaque; (b) theoretical radial strain distributions along the vertical and horizontal lines specified on (a); (c) radial strain elastogram as computed with the LSME; (d) LSME radial strain distributions along the vertical and horizontal lines specified in (c). The color bars express the strain in percent.

Cheng *et al.*, 1993; Lee *et al.*, 1993; Ohayon *et al.*, 2001; Williamson *et al.*, 2003). However, the kinetics reported here were achieved with small pressure gradients (around 15 mm Hg) such that the radial strain remained below 10%. The Newton–Raphson iterative method with a residual nodal tolerance of 4×10^{-4} N was used to solve the FE models. The calculations were performed with a number of elements close to 7200.

This computational structural FE analysis was used to perform the kinematics of the vascular tissue. The dynamic image-formation model [Eq. (16)] was implemented using the Matlab software (The MathWorks Inc, MA, USA, ver.

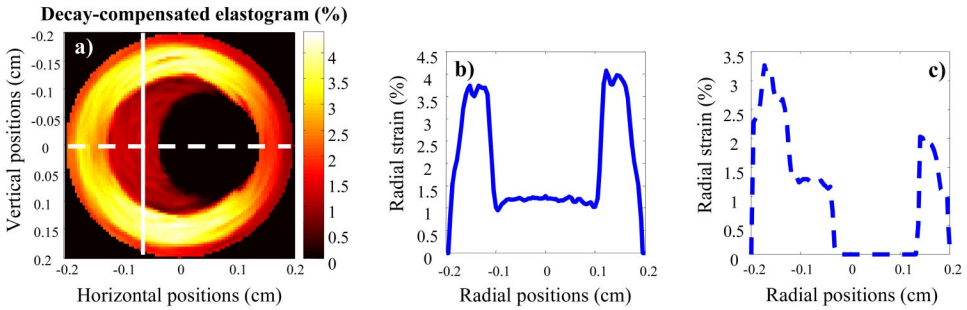

FIG. 7. (a) Strain-decay-compensated LSME elastogram, showing substantial contrast improvement between hard and soft materials; (b) vertical 1-D plot from the elastogram showing a contrast ratio close to 3 between the plaque and the normal vascular tissue, as can be expected; (c) horizontal 1-D plot from the elastogram, showing effective strain decay compensation, and thus a substantial improvement of the contrast ratio. The color bar expresses the strain in percent.

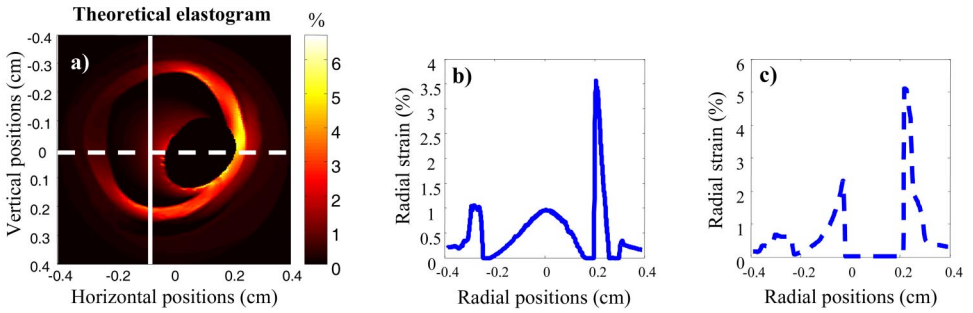

FIG. 8. (a) Theoretical radial strain elastogram for the real plaque, showing very complex strain patterns; (b) and (c) show vertical and horizontal 1-D plots from the elastogram, respectively. Strain decay is specifically observed at the inner portion of the vessel wall. The color bar expresses the strain in percent.

6.0). The process to simulate polar radio-frequency (rf) images is schematically presented in Fig. 5, for a homogeneous (pathology-free) vessel wall. It can be summarized as follows. It started by generating in Matlab a scattering function that simulated the acoustical characteristics of a transverse vascular section in Cartesian coordinates, $z'(x,y)$. The axial and lateral displacement fields were computed with Ansys and were applied upon $z'(x,y)$ to perform motion and then to provide $z'_{LT^{-1}}(x,y)$.[g]

The next step consisted in mapping $z'(x,y)$ and $z'_{LT^{-1}}(x,y)$ in a polar coordinate system (r,φ) to provide $z(r,\varphi)$ and $z_{LT_p^{-1}}(r,\varphi)$ [Eqs. (15) and (16)]. Both polar-mapped acoustic impedance functions were then convolved with the polar PSF $h(r,\varphi)$ to provide polar pre- and post-tissue-motion rf images [$I(r,\varphi,0)$ and $I(r,\varphi,t)$, given by Eq. (16)]. Those images were used as inputs to the LSME [Eq. (19)].

In summary, the static and the dynamic image-formation models associated with a polar scan were derived in Sec. II A, whereas the LSME was adapted for EVE in Sec. II B. In Sec. III, this new approach is validated using the biomechanical simulations of the vessel wall kinematics (for the ''ideal'' and the ''realistic'' plaque geometries) presented in Sec. II C. Indeed, radial elastograms (ϵ_{rr}), computed from simulated rf data with the LSME, are compared with ''theoretical'' ϵ_{rr} obtained with Ansys FE software. For the purpose of that study, a noise term was added to the rf data to simulate electronic noise. The signal-to-noise ratio was 20 dB.

III. RESULTS

The *idealized* vessel of Fig. 3 measured about 3.8 mm in the outer diameter, whereas the rf images extended to 4 mm×4 mm. The *real case* vessel of Fig. 4(b) measured about 7 mm in the outer diameter, whereas the rf images extended to 8 mm×8 mm. For the purpose of simulations, the intraluminal pressure gradients were set at 15.79 mm Hg and 11.73 mm Hg for the *idealized* and the *realistic* vessels, respectively. According to that, the dilation at the inner wall was around 7%[h] in both cases. The PSF characterized a 20 MHz central frequency transducer, as described in the forward problem (Sec. II A). The LSME (described in Sec. II B) was implemented to assess tissue motion. Measurement-windows of 0.38 mm×0.40 mm and 0.77 mm×0.80 mm, with 90% axial and lateral overlaps, were used for the idealized and the realistic cases, respectively. For more details concerning the definition of the measurement-window required with the LSME, the reader is referred to Fig. 1 of Maurice *et al.* (2004).

A. Investigation of the "ideal" plaque pathology

Figure 6(a) presents the theoretical radial strain elastogram, computed for the ''ideal'' pathology case, using Ansys FE software. The plaque can slightly be differentiated from the normal vascular tissue, whereas a region of higher strain values is observed at the right portion of the inner vessel wall. This ''mechanical artifact'' is a direct consequence of the well known strain decay phenomenon[i] (Shapo *et al.*, 1996a). For a more quantitative illustration, plots from the theoretical elastogram for two orthogonal orientations along x and y are presented in Fig. 6(b). Indeed, the vertical plot (—) shows low contrast between the plaque and the normal vascular tissue, whereas the horizontal plot (---) clearly points out the presence of strain decay.

Figure 6(c) presents the radial strain elastogram as computed with the LSME, using simulated rf images. As for the theoretical elastogram in Fig. 6(a), the plaque is slightly distinguishable from the normal vascular tissue. The plots of Fig. 6(d) confirm such an observation. Note that lower strain values were computed in the LSME elastogram than in theory, specifically at the inner wall. That strain underestimation in the regions close to the lumen is due to the windowing process required to assess tissue motion with the LSME.

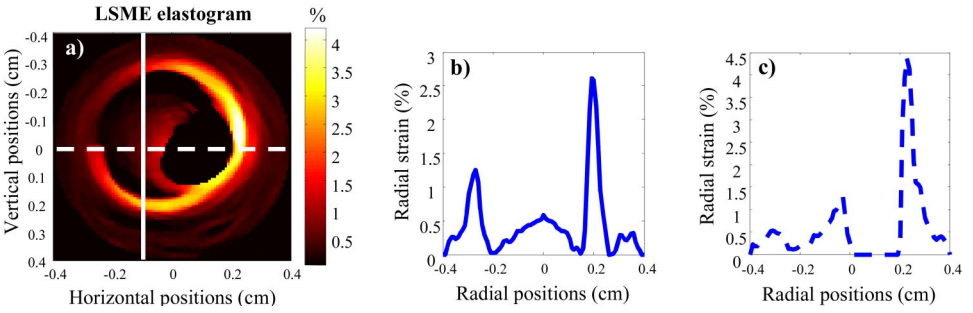

FIG. 9. (a) Radial strain elastogram as computed with the LSME for the real plaque; (b) and (c) vertical and horizontal 1-D plots from the elastogram, respectively. Because of strain decay, there is not a clear demarcation between cellular and dense fibroses, specifically in (c). The color bar expresses the strain in percent.

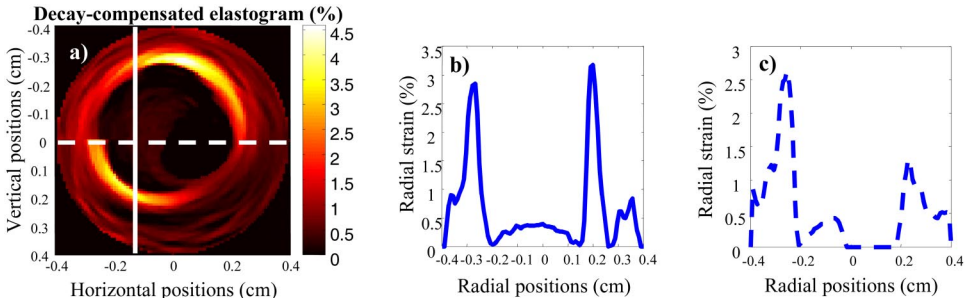

FIG. 10. (a) Strain-decay-compensated LSME elastogram for the real plaque, showing a substantial contrast improvement; (b) and (c) vertical and horizontal 1-D plots from the elastogram showing more effective contrast ratio between dense and cellular fibroses, after strain decay compensation. The color bar expresses the strain in percent.

Moreover, the maximum strain can be observed at the inner boundary around 1 and 5 o'clock. Such a softening artifact is a consequence of stress concentration at the interface between hard (plaque) and softer (normal) materials.

For the purpose of compensating for strain decay, the LSME radial strain elastogram was post-processed. Indeed, ϵ_{rr} was modulated with a function proportional to the square of the vessel radius.[j] In Fig. 7(a) is presented the strain-decay-compensated LSME elastogram, showing substantial contrast improvement. For instance, the axial plot of Fig. 7(b) shows an effective contrast ratio close to 3 between the plaque and the normal vascular tissue, as it can be expected. Equivalently, Fig. 7(c) also shows some valuable contrast ratio improvement.

B. Investigation of a "realistic" vessel wall pathology

Figure 8(a) presents the theoretical radial strain elastogram, computed for the "realistic" pathology case. Interestingly, complex strain patterns are observed; nevertheless, different regions can be identified. For instance, since the ratio of Young's moduli between the dense and the cellular fibroses was set to 10, both of those materials can be distinguished. Less contrast is seen between the cellular fibrosis and the healthy vascular tissue because their Young's modulus contrast was set to 3. As illustrated with vertical and horizontal 1-D plots from the elastogram [Figs. 8(b) and 8(c), respectively], strong strain decay is observed specifically at the inner portion of the vessel wall.

Figure 9(a) presents the radial strain elastogram as computed with the LSME, using simulated rf images. As for the theoretical elastogram in Fig. 8(a), very complex strain patterns are observed. Moreover, the dense and the cellular fibrosis tissues can be identified. However, while less prominent than in the "ideal" case study, strain decay remains a significant factor to compensate for improved image interpretation. This is illustrated in Figs. 9(b) and 9(c), where vertical and horizontal 1-D plots from the elastogram are presented. Whereas low strain values clearly indicate the presence of stiff materials in Fig. 9(b), this is not the case in Fig. 9(c).

In Fig. 10(a) is presented the strain-decay-compensated LSME elastogram, showing substantial contrast improvement. Now, the vertical plot [Fig. 10(b)] as well as the horizontal one [Fig. 10(c)] show a more effective contrast ratio between dense and cellular fibroses, and between cellular fibrosis and the normal vascular tissue. Moreover, it is interesting to notice the presence of moderate strain values (around 0.6 to 0.8%) at the extremities of the plots; this characterizes regions of healthy vascular tissue, namely the media and adventicia.

IV. DISCUSSION

Pathological conditions of vascular tissues often induce changes in the vessel wall elasticity. For instance, plaque deposit stiffens the vascular wall and then counteracts its dilation under systolic blood pressure. Hence, investigating mechanical and elastic properties of the arteries seems to be a suitable method to appreciate the dynamics of the arterial wall and its pathologies. In this paper, a model-based approach devoted to outline the elastic properties of the vessel wall with endovascular elastography (EVE) was presented. Results obtained from numerical simulations establish the potential of such a method to reliably assess strain patterns from very complex arterial and plaque structures.

A. About the forward problem

Regarding the forward problem in EVE, a polar static image-formation model was introduced. Taking into account the ultrasound beam divergence associated with high-frequency sector scans, this image-formation model was formulated using the superposition integral. The radial variation was conveyed with the beam width, which increases as a linear function of depth. This is actually a relatively simplistic approximation. In practice, the transducer point-spread function (PSF) is expected to be more complex. For example, the acoustic wavefronts may be nonplanar, and Eq. (4) (an approximation of the far field PSF) does not hold anymore. Since it was demonstrated that such complex wavefronts can induce speckle motion artifacts (Kallel and Bertrand, 1994; Maurice and Bertrand, 1999b), it would be worthwhile, in the future, to address the polar dynamic image-formation model with a more complex ("realistic") PSF geometry.

B. About the tissue motion estimation

To assess tissue motion, the Lagrangian speckle model estimator (LSME) was used. The LSME is a 2-D model-based estimator that allows computing the full 2-D deformation matrix Δ of Eq. (10) (Δ is directly assessed; no derivative of the displacement fields is required with this method). In this paper, it was adapted for EVE investigations. While the full 2-D polar deformation matrix $\xi(t)$ of Eq. (13) was assessed, only the radial strain component $\xi_{rr}(=\epsilon_{rr})$ was displayed. This was motivated by the fact that tissue motion,

in EVE, is expected to run parallel with the ultrasound beam. Interestingly, the method was implemented through an adapted version of the Levenberg-Marquardt minimization algorithm, using the optical flow equations to compute the Jacobbian matrix. The theoretical framework was validated using the biomechanical simulations of the vessel wall kinematics for an ''ideal'' and a ''realistic'' plaque geometries, respectively. Elastograms, computed from simulated rf data with the LSME, were supported by ''theoretical'' ones provided by Ansys FE software.

V. CONCLUSION

A new method to characterize mechanically complex vascular pathologies in endovascular elastography (EVE) was presented. First, a polar static image-formation model was introduced. The radial variation of the PSF, associated with the high-frequency IVUS instrument, was conveyed with the beam width, which increases as a linear function of depth. Second, the Lagrangian speckle model estimator (LSME) was adapted for EVE investigations. The LSME was formulated as a nonlinear minimization problem, for which an analytical formulation of the Jacobian matrix was derived. The hypothesis behind that model-based approach was that speckle can be seen as a material property. While the full 2-D polar strain tensor was assessed, only the radial elastograms were presented. Elastograms, computed with the method from simulated rf data of pathological vessel walls, were supported by theoretical ones provided by Ansys FE software. The results help to provide confidence in the potential of EVE to provide very useful information about the heterogeneous nature of atherosclerotic plaques.

ACKNOWLEDGMENTS

The authors gratefully acknowledge Dr. David Savéry for reviewing the manuscript, Mr. François Treyve for helping in numerical simulations with Ansys, and Ms. Isabelle Fontaine and Dr. Michel Bertrand for very helpful discussions. This work was supported by grants from the Natural Sciences and Engineering Research Council of Canada (#138570-01) and Valorisation-Recherche Québec (structuring group program). The salary of Dr. Cloutier is partially supported by a National Scientist award from the Fonds de la Recherche en Santé du Québec.

APPENDIX A: THE LEVENBERG-MARQUARDT NONLINEAR MINIMIZATION

$I_{\mathrm{Lag}}(r,\varphi,t)$ and $\Re(r,\varphi,t)$ [Eq. (19)] are implicit functions of θ_i [Eq. (9)]. For clarity and without loss of generality, let us rewrite $I_{\mathrm{Lag}}(r,\varphi,t)$ as $I_{\mathrm{Lag}}(\vec{\theta})$ and $\Re(r,\varphi,t)$ as $\Re(\vec{\theta})$, respectively; $\vec{\theta}$ is the vectorization of $[LT_p]$. At the kth iteration, one will have

$$\begin{aligned}\Re(\vec{\theta}^k) &= \Re(\vec{\theta}^{k-1}+\Delta\vec{\theta}^k)\\ &= I_0 - I_{\mathrm{Lag}}(\vec{\theta}^{k-1}) - \sum_j^n \frac{\partial I_{\mathrm{Lag}}}{\partial\theta_j}\Delta\theta_j^k|_{\theta_j^{k-1}},\end{aligned} \tag{A1}$$

with $I_0 = I(r,\varphi,0)$.

In Eq. (A1), $\vec{\theta}^{k-1}$ is computed at iteration $k-1$, $\Delta\theta_j^k$ is the increment of the jth component of $\vec{\theta}$, $I_{\mathrm{Lag}}(\vec{\theta}^{k-1})$ is the Lagrangian image at iteration $k-1$, and $\partial I_{\mathrm{Lag}}/\partial\theta_j$ are partial derivatives of I_{Lag} with respect to each component of $\vec{\theta}$. A more compact formulation of Eq. (A1) is given as

$$\vec{I}_0 - \vec{I}_{\mathrm{Lag}}(\vec{\theta}^{k-1}) = [J_{k-1}]\overrightarrow{\Delta\theta}^k + \vec{\Re},$$

with

$$J_{k-1} = \begin{bmatrix} \frac{\partial I_{\mathrm{Lag}}}{\partial\theta_1} & \frac{\partial I_{\mathrm{Lag}}}{\partial\theta_2} & \cdots & \frac{\partial I_{\mathrm{Lag}}}{\partial\theta_n} \\ \vdots & \vdots & & \vdots \\ \frac{\partial I_{\mathrm{Lag}}}{\partial\theta_1} & \frac{\partial I_{\mathrm{Lag}}}{\partial\theta_2} & \cdots & \frac{\partial I_{\mathrm{Lag}}}{\partial\theta_n} \end{bmatrix}, \tag{A2}$$

where $\vec{I}_0$, $\vec{I}_{\mathrm{Lag}}(\vec{\theta}^{k-1})$, and $\vec{\Re}$ are vectorizations of I_0, I_{Lag}, and $\Re$, respectively; $[J_{k-1}]$ is the Jacobian matrix; and $\overrightarrow{\Delta\theta}^k$ is a vector of increments used to update the Lagrangian images ($\overrightarrow{\Delta\theta}^k$ is also known in the literature as the step size). For such a model, the least-square error solution is given as

$$\Delta\theta^k = [J_{k-1}^T J_{k-1}]^{-1} J_{k-1}^T (\vec{I}_0 - \vec{I}_{\mathrm{Lag}}(\vec{\theta}^{k-1})), \tag{A3}$$

where the subscript T designates the transpose operator. When $J_{k-1}^T J_{k-1}$ is not invertible, a regularized version of Eq. (A3) may be required to ensure the convergence of the solution. The Levenberg-Marquardt method (L&M) converges to a potential solution for such a problem (Levenberg, 1963; Marquardt, 1944). The L&M regularized inversion was implemented as

$$\overrightarrow{\Delta\theta}^k = [J_{k-1}^T J_{k-1} + \lambda_k I]^{-1} J_{k-1}^T (\vec{I}_0 - \vec{I}_{\mathrm{Lag}}(\vec{\theta}^{k-1})), \tag{A4}$$

where λ_k is a non-negative scalar, and I is the identity matrix.

APPENDIX B: THE OPTICAL FLOW EQUATIONS AND THE JACOBIAN MATRIX

$I_{\mathrm{Lag}}(\vec{\theta}^{k-1})$ can be seen as a function that describes a material property. Assuming that such a material property is preserved with motion, the total derivative of $I_{\mathrm{Lag}}(\vec{\theta}^{k-1})$ can be expressed as

$$\begin{aligned}\frac{dI_{\mathrm{Lag}}(\vec{\theta}^{k-1})}{d\theta_i} &= \frac{\partial I_{\mathrm{Lag}}(\vec{\theta}^{k-1})}{\partial r}\frac{dr}{d\theta_i} + \frac{\partial I_{\mathrm{Lag}}(\vec{\theta}^{k-1})}{\partial\varphi}\frac{d\varphi}{d\theta_i}\\ &\quad + \frac{\partial I_{\mathrm{Lag}}(\vec{\theta}^{k-1})}{\partial\theta_i} = 0\\ \therefore\ \frac{\partial I_{\mathrm{Lag}}(\vec{\theta}^{k-1})}{\partial\theta_i} &= -\frac{\partial I_{\mathrm{Lag}}(\vec{\theta}^{k-1})}{\partial r}\frac{dr}{d\theta_i}\\ &\quad - \frac{\partial I_{\mathrm{Lag}}(\vec{\theta}^{k-1})}{\partial\varphi}\frac{d\varphi}{d\theta_i},\end{aligned} \tag{B1}$$

with

$$\frac{\partial I_{\mathrm{Lag}}(\vec{\theta}^{k-1})}{\partial\vec{\theta}} = I_{\mathrm{Lag}}(\vec{\theta}^{k-1}+\overrightarrow{\Delta\theta}^k) - I_{\mathrm{Lag}}(\vec{\theta}^{k-1}).$$

As introduced in the paper (section II B2), under the assumption of a small ROI $(\Delta r,\Delta\varphi)$ that is far from the vessel lumen center, tissue motion equivalently can be inves-

tigated using either the Cartesian or polar coordinates. Additionally, for small motion, the gradient of $I_{\mathrm{Lag}}(\vec{\theta}^{k-1})$ should not be significantly different from the gradient $I(r,\varphi,0)$. These hypotheses, in conjunction with Eq. (9), lead to

$$\frac{\partial I_{\mathrm{Lag}}(\vec{\theta}^{k-1})}{\partial \vec{\theta}} \cong \frac{\partial I(\vec{\theta}^{k-1})}{\partial \vec{\theta}} = -\left\{ \frac{\partial I}{\partial x}, \frac{\partial I}{\partial x}x, \frac{\partial I}{\partial x}y, \frac{\partial I}{\partial y}, \frac{\partial I}{\partial y}x, \frac{\partial I}{\partial y}y \right\}. \quad \text{(B2)}$$

Eq. (B2) gives the full expression for the 6 components of the Jacobian matrix $[J_{k-1}]$ [Eq. (21)].

[b)]The radial position-dependence of the PSF is associated with the divergence and the attenuation of the high-frequency IVUS instrument with depth. The attenuation was not taken into account in this study.

[c)]Whereas the lumen is in practice in the near field, it is here simulated as being in the far field [with a beam width $\sigma_{\varphi}(r)=\sigma_0$]. This simplifying hypothesis does not alter the generality of the model, since motion assessment is not relevant for the lumen.

[d)]$[LT]$ is used to define rotation as well as nonrigid motion due to compression, expansion, or shearing.

[e)]Adenosine triphosphate (ATP) temporarily (<3 sec) stops cardiac pulsations. During that period, the blood pressure decreases at approximately 20 mm Hg, allowing the acquisition of data at an optimum unload state of the arterial wall.

[f)]An alternative could have been the simulation of a softer surrounding tissue (about 100 kPa). Since the objective of those simulations was to obtain strain values in the range of 0–10% approximately, this would have required decreasing the nominal intraluminal pressure gradient such that the dilation at the inner wall remained below 10% to prevent signal decorrelation.

[g)]It is to note that $z'(x,y)$ was low-pass filtered with a 2-D-circular Gaussian filter having a 1-pixel standard deviation. Such a step was required in order to reduce the interpolation noise introduced when resampling $z'(x,y)$ to provide $z'_{LT^{-1}}(x,y)$.

[h)]Referring to ϵ_{rr} computed with Ansys FE software (Figs. 6 and 8), the maximum radial strain for both cases was close to 6%. Such a small amount of strain was required to prevent signal decorrelation. In practice, this can be achieved by acquiring pre- and post-motion rf images near end-diastole (de Korte *et al.*, 2000b).

[i)]Radial strain ϵ_{rr} is proportional to $1/r^2$. This decreasing of ϵ_{rr} with depth is usually defined as strain decay.

[j)]Since radial strain ϵ_{rr} decreases proportionally to $1/r^2$, the compensation for strain decay consists in multiplying ϵ_{rr} by a function proportional to r^2, with respect to the vessel lumen center.

Bamber, J. C., and Dickinson, R. J. (**1980**). ''Ultrasonic B-scanning: A computer simulation,'' Phys. Med. Biol. **25**, 463–479.

Brusseau, E., Fromageau, J., Finet, G., Delachartre, P., and Vray, D. (**2001**). ''Axial strain imaging of intravascular data: Results on polyvinyl alcohol cryogel phantoms and carotid artery,'' Ultrasound Med. Biol. **27**, 1631–1642.

Chaturvedi, P., Insana, M. F., and Hall, T. J. (**1998a**). ''2-D companding for noise reduction in strain imaging,'' IEEE Trans. Ultrason. Ferroelectr. Freq. Control **45**, 179–191.

Chaturvedi, P., Insana, M. F., and Hall, T. J. (**1998b**). ''Testing the limitations of 2-D companding for strain imaging using phantoms,'' IEEE Trans. Ultrason. Ferroelectr. Freq. Control **45**, 1022–1031.

Cheng, G. C., Loree, H. M., Kamm, R. D., Fishbein, M. C., and Lee, R. T. (**1993**). ''Distribution of circumferential stress in ruptured and stable atherosclerotic lesions: a structural analysis with histopathological correlation,'' Circulation **87**, 1179–1187.

de Korte, C. L., Pasterkamp, G., Van der Steen, A. F. W., Woutman, H. A., and Bom, N. (**2000a**). ''Characterization of plaque components with intravascular ultrasound elastography in human femoral and coronary arteries in vitro,'' Circulation **102**, 617–623.

de Korte, C. L., Van der Steen, A. F. W., Céspedes, E. I., Pasterkamp, G., Carlier, S. G., Mastik, F., Schoneveld, A. H., Serruys, P. W., and Bom, N. (**2000b**). ''Characterization of plaque components and vulnerability with intravascular ultrasound elastography,'' Phys. Med. Biol. **45**, 1465–1475.

de Korte, C. L., Van der Steen, A. F. W., Céspedes, E. I., and Pasterkamp, G. (**1998**). ''Intravascular ultrasound elastography in human arteries: Initial experience in vitro,'' Ultrasound Med. Biol. **24**, 401–408.

de Korte, C. L., Céspedes, E. I., Van der Steen, A. F. W., and Lancée, C. T. (**1997**). ''Intravascular elasticity imaging using ultrasound—Feasibility studies in phantoms,'' Ultrasound Med. Biol. **23**, 735–746.

Horn, B. K. P. (**1986**). Robot Vision (*McGraw-Hill*, New York), pp. 278–298.

Kallel, F., and Bertrand, M. (**1994**). ''Speckle motion artifact under tissue rotation,'' IEEE Trans. Ultrason. Ferroelectr. Freq. Control **41**, 105–122.

Lee, R. T., Loree, H. M., Cheng, G. C., Lieberman, E. H., Jaramillo, N., and Schoen, F. J. (**1993**). ''Computational structural analysis based on intravascular ultrasound imaging before in vitro angioplasty: prediction of plaque fracture locations,'' J. Am. Coll. Cardiol. **21**, 777–782.

Levenberg, K. (**1963**). ''A method for the solution of certain non-linear problems in least-squares,'' Q. Appl. Math **2**, 164–168.

Loree, H. M., Kamm, R. D., Stringfellow, R. G., and Lee, R. T. (**1992**). ''Effects of fibrous cap thickness on peak circumferential stress in model atherosclerotic vessels,'' Circ. Res. **71**, 850–858.

Marquardt, D. W. (**1944**). ''An algorithm for least-squares estimation of non-linear parameters,'' J. Soc. Ind. Appl. Math. **11**, 431–441.

Maurice, R. L., Ohayon, J., Frétigny, Y., Bertrand, M., Soulez, G., and Cloutier, G. (**2004**). ''Non-invasive vascular elastography: Theoretical framework,'' IEEE Trans. Med. Imaging **23**, 164–180.

Maurice, R. L., and Bertrand, M. (**1999a**). ''Lagrangian speckle model and tissue-motion estimation—Theory,'' IEEE Trans. Med. Imaging **18**, 593–603.

Maurice, R. L., and Bertrand, M. (**1999b**). ''Speckle-motion artifact under tissue shearing,'' IEEE Trans. Ultrason. Ferroelectr. Freq. Control **46**, 584–594.

Meunier, J., and Bertrand, M. (**1995**). ''Ultrasonic texture motion analysis: Theory and simulation,'' IEEE Trans. Med. Imaging **14**, 293–300.

Ohayon, J., Teppaz, P., Finet, G., and Rioufol, G. (**2001**). ''In vivo prediction of human coronary plaque rupture location using intravascular ultrasound and finite element method,'' Coron. Artery Dis. **12**, 655–663.

Ophir, J., Alam, S. K., Garra, B., Kallel, F., Konofagou, E., Krouskop, T., and Varghese, T. (**1999**). ''Elastography: ultrasonic estimation and imaging of the elastic properties of tissues,'' Proc. Inst. Mech. Eng. **213**, 203–233.

Rachev, A. (**1997**). ''Theoretical study of the stress-dependent remodeling on arterial geometry under hypertensive conditions,'' J. Biomech. **30**, 819–827.

Rioufol, G., Finet, G., Tabib, A. *et al.* (**1999**). ''The (often) four-layer apparence of coronary arteries by intravascular ultrasound: the tunica adventitia,'' J. Am. Coll. Cardiol. **16**, 77A (abstract).

Ryan, L. K., and Foster, F. S. (**1997**). ''Ultrasonic measurement of differential displacement strain in a vascular model,'' Ultrason. Imaging **19**, 19–38.

Shapo, B. M., Crowe, J. R., Skovoroda, A. R., Eberle, M. J., Cohn, N. A., and O'Donnell, M. (**1996a**). ''Displacement and strain imaging of coronary arteries with intraluminal ultrasound,'' IEEE Trans. Ultrason. Ferroelectr. Freq. Control **43**, 234–246.

Shapo, B. M., Crowe, J. R., Erkamp, R., Emelianov, S. Y., Eberle, M. J., and O'Donnell, M. (**1996b**). ''Strain imaging of coronary arteries with intraluminal ultrasound: Experiments on an inhomogeneous phantom,'' Ultrason. Imaging **18**, 173–191.

Treyve, F., Ohayon, J., Finet, G., and Rioufol, G. (**2003**). ''Modelling of the stress distribution in an atherosclerotic plaque in man using a finite element analysis,'' Comptes Rendus Mécanique **331**, 449–454.

Wan, M., Li, Y., Li, J., Cui, Y., and Zhou, X. (**2001**). ''Strain imaging and elasticity reconstruction of arteries based on intravascular ultrasound video images,'' IEEE Trans. Biomed. Eng. **48**, 116–120.

Williamson, S. D., Lam, Y., Younis, H. F., Huang, H., Patel, S., Kaazempur-Mofrad, M. R., and Kamm, R. D. (**2003**). ''On the sensitivity of wall stresses in diseased arteries to variable material properties,'' J. Biomech. Eng. **125**, 147–155.